



# OPEN Cold storage surpasses the impact of biological age and donor characteristics on red blood cell morphology classified by deep machine learning

Yuanheng Zhao<sup>1</sup>, Mackenzie Brandon-Coatham<sup>2</sup>, Mahsa Yazdanbakhsh<sup>1</sup>, Olga Mykhailova<sup>2</sup>, Nishaka William<sup>1</sup>, Rafay Osmani<sup>1</sup>, Tamir Kanias<sup>3,4</sup> & Jason P. Acker<sup>1,2</sup>✉

Assessment of the morphology of red blood cells (RBCs) can improve clinical benefits following blood transfusion. Deep machine learning surpasses traditional microscopy-based classification methods, offering more accurate and consistent results while reducing time and labor intensity. RBCs from teenage males, teenage females, senior males, and senior females were biologically age-profiled or density-separated into dense/old RBCs (O-RBCs) and less-dense/young (Y-RBCs) throughout hypothermic storage and assessed using image flow cytometry with deep machine learning analysis. Regardless of biological age, morphology index decreased with hypothermic storage. Significant differences in RBC morphology index were not seen when comparing unseparated RBCs (U-RBCs), O-RBCs, and Y-RBCs, although the proportions of morphology subclasses revealed differences between RBCs groups from different donor groups and in samples with different biological age. Cold storage remains the most significant influence on morphology, although teenage male donors demonstrated slightly more susceptibility to storage lesions compared with senior males and females. Our work highlights that hypothermic storage most significantly impacts RBC morphology over biological age and donor characteristics, emphasizing the importance of storage effects on transfusion quality and safety.

**Keywords** Red blood cells, Morphology, Storage lesion, Donor factors, Biological age, Machine learning

Transfusion medicine is a life-saving treatment for patients suffering severe blood loss or anemia due to cancers and other blood diseases or disorders<sup>1–3</sup>. Red blood cells (RBCs) are the most frequently transfused blood product with approximately 113 million units being administered worldwide per year<sup>4,5</sup>. Assessment of blood product quality has continued to improve the clinical benefits of blood transfusion by reducing the risks of adverse transfusion outcomes such as hemolytic and immune-mediated reactions<sup>6</sup>. RBC quality can be assessed in a variety of ways, ranging from biochemical/biophysical assays to expert interpretation of microscopic images<sup>7</sup>. Storage of RBCs in closed blood bag systems results in an accumulation of hypothermic storage lesions consisting of biochemical and morphological changes<sup>1,7–10</sup>. Previous reports have shown that loss of membrane integrity causes reversible morphological changes in RBCs from regular biconcave discocytes (smooth and crenated discs) into echinocytes (crenated discoid and spheroid), and that echinocytes can further degrade irreversibly into spherocytocytes (crenated spheres and smooth spheres)<sup>10–12</sup>. These changes can be used to characterize the aging of RBCs during storage by assessing the distribution of fresh, younger RBCs (Y-RBCs) and senescent, older RBCs (O-RBCs) in donated blood products<sup>8,13</sup>. RBC morphology has also provided insights into the biomechanical alterations occurring in RBCs that lead to changes in their deformability and osmotic fragility<sup>14,15</sup>. Classically, the morphology of RBCs can be divided into six subclasses: smooth disc, crenated disc, crenated discoid, crenated spheroid, crenated sphere, and smooth sphere, with the three older subclasses (crenated spheroids, crenated spheres, and smooth spheres) consisting of smaller, older RBCs, being collectively

<sup>1</sup>Department of Laboratory Medicine and Pathology, University of Alberta, Edmonton, AB, Canada. <sup>2</sup>Innovation and Portfolio Management, Canadian Blood Services, Edmonton, AB, Canada. <sup>3</sup>Vitalant Research Institute, Denver, CO, USA. <sup>4</sup>Department of Pathology, University of Colorado Denver Anschutz Medical Campus, Aurora, CO, USA. ✉email: jason.acker@blood.ca

defined as storage-induced micro-erythrocytes (SMEs)<sup>15</sup>. Roussel et al. determined the proportion of SMEs in RBC concentrates during storage and its correlation with transfusion recovery, showing that quantification of accumulated SMEs has the potential to improve blood product quality assessment<sup>15</sup>. Examination of RBC morphology by microscopy has traditionally been assessed by highly-trained experts with ample hematology experience<sup>16,17</sup>. Briefly, when the microscopic approach to RBC morphology assessment is taken, blood samples are spread on slides for manual cell counting and relative fractions of the RBC subclasses are calculated. However, this process has several limitations including that it is labor-intensive, prone to subjective bias, and limited by small sample sizes, all of which potentially lead to inaccuracies in the final quality outcomes reported<sup>11</sup>. It would be beneficial for clinical use to simplify and automate this examination process by exploring novel technological advances and high-throughput computation<sup>11,12</sup>. Artificial intelligence (AI) presents a potential solution to improving RBC morphological assessment, as its efficacy and benefits are already being explored and evaluated in various medical fields, particularly pathology and radiology<sup>11,18–20</sup>.

Deep machine learning, a powerful subset of AI, refers to a multilayered network of artificial neurons aimed at creating models from raw data to automatically detect patterns and perform tasks, such as detection and classification, in various domains<sup>21,22</sup>. This advancement has the potential to be applied to the morphological assessment of RBCs. Together, with imaging flow cytometry (IFC) technology which employs the high-throughput nature of flow cytometry together with the ability to capture multi-channel fluorescent images of single cells, there exists the potential for the development of a statistically robust and automated classification workflow for analysis of RBC images<sup>23,24</sup>. Several groups have successfully applied deep machine learning to single-cell RBC images previously to perform supervised cell classification and weakly supervised learning<sup>23,25</sup>. Doan et al. developed a deep learning framework for the assessment of the morphology of single RBC images, in which the neural network learned the morphological properties of RBCs independently from visual categories defined by experts<sup>23</sup>. The deep learning analysis pipeline employed by Doan et al. included pre-processing, training a classification model, evaluation of the trained model, and prediction of the classification of unlabeled data<sup>11,23</sup>. Doan et al. applied the developed deep machine learning and assessed the quality of stored RBCs, but did not study RBC biological age and storage lesion within the context of other donor-related factors, such as sex and age<sup>23</sup>.

While the changes to RBCs resulting from hypothermic storage-induced biochemical and structural alterations (i.e. oxidative stress, protein / lipid modifications, and cytoskeletal changes), that lead to increased rigidity, loss of water, and cellular constituents are well documented<sup>26–28</sup>, the differences in the storage lesions experienced by various RBC subpopulations have only emerged more recently. At the time of donation, donor products consist of a heterogeneous population of RBCs as the natural aging process creates a diverse population of RBCs with varying biological ages from old to young in circulation, affecting RBC quality<sup>7,13</sup>. Furthermore, studies have shown that, at the blood collection stage, donor characteristics such as age, sex, and number of previous blood donations can also have an impact on the quality of RBCs, morphology included<sup>7,13</sup>. RBCs from male donors have been found to have cells of older biological age<sup>13</sup> that contribute more to the storage lesion with poorer blood quality than cells from female donors<sup>7</sup>. The morphological differences between RBCs of various biological ages in the context of different donor ages and sex across storage has not yet been examined.

In this work, RBC morphology over hypothermic storage (day 5, 14, 28, and 42) and in the context of RBC biological age, as well as the donor characteristics of age (teenage, senior) and sex (male, female) were assessed, using deep machine learning (Fig. 1) to classify unlabeled images of RBCs from 60 donors. Previously, donor age was shown to be more of a crucial factor affecting RBC deformability when compared with donor sex and RBC biological age<sup>8,13</sup>, therefore we hypothesized that the teenage male, senior male donor groups, older biological age (O-RBCs), and longer hypothermic storage, would demonstrate poorer morphology or lower morphology index (MI), during storage.

## Results

### Trained machine learning model is reliable for RBC morphology prediction

The training accuracy of the deep machine learning model to the manually labeled database was monitored in real-time and found to remain relatively stable (over 80%) as the training process and iterations increased (Fig. S1a). Against the training dataset, the accuracy of the model was 96.40%. Also, against the testing data set (20% of the manually labeled dataset split from the database), the model's accuracy was 96.70%. Additionally, we iteratively evaluated the trained model using three additional manually labeled datasets, and the accuracy of the trained model was assessed to be  $84.17 \pm 4.32\%$ . A representative evaluation result indicating the number of images in each morphology subclass and the corresponding confusion matrix is shown in Figs. S1b and S1c, respectively. These evaluated accuracies are acceptable, as machine learning models with over 70% accuracy are generally considered suitable for practical use<sup>29,30</sup>. Based on the evaluation results associated with the performance of the trained model, it reliably analyzed RBC images to predict morphology subclasses.

### U-RBC morphology results obtained by deep machine learning model show correlation with storage hemolysis

To demonstrate the reliability of our model's predictions, we compared it against RBC hemolysis, a well-established quality parameter sensitive to storage conditions. We assessed the relationship between storage hemolysis and MIs within U-RBCs across all donor groups. For senior female donors, the correlation between hemolysis and MIs increased significantly over storage with the highest  $R^2$  value observed on Day 28 ( $R^2 = 0.7032$ ) (Table 1), indicating a strong inverse correlation. However, this relationship weakened by Day 42 ( $R^2 = 0.3898$ ) (Fig. 2d). A similar trend was observed in senior male donors, where the strongest correlation was also found on Day 28 ( $R^2 = 0.6108$ ) (Fig. 2c), but this weakened by Day 42 ( $R^2 = 0.1747$ ). In contrast, the correlation between hemolysis and MIs in teenage females and males was generally weaker compared to senior groups. For teenage

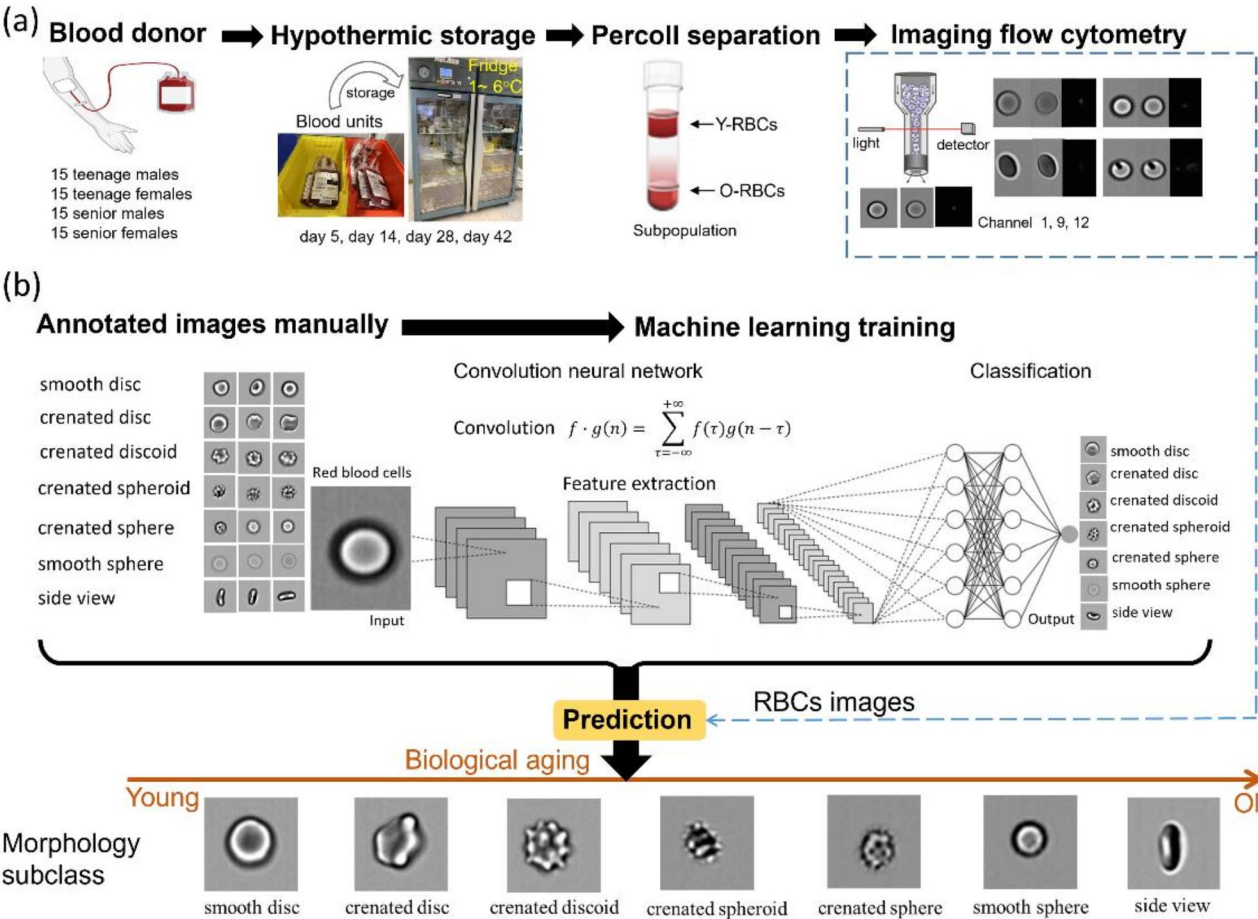


**Fig. 1.** Study design for a deep machine learning approach to RBC morphology classification. (a) Sample and image preparation. (b) Flowchart of the data analysis pipeline utilized to conduct the supervised learning for the distinction of RBC morphology subclasses.

Donor characteristics	Relationship in U-RBCs	Day 5	Day 14	Day 28	Day 42
Teenage Male (TM)	Hemolysis vs. MI	0.0862	0.0346	0.4754	0.2748
	Hemolysis vs. SMEs	0.0053	0.1270	0.5261	0.4139
Teenage Female (TF)	Hemolysis vs. MI	0.0366	0.0133	0.1657	0.0656
	Hemolysis vs. SMEs	0.0221	0.0071	0.0079	0.1446
Senior Male (SM)	Hemolysis vs. MI	0.2001	0.1369	0.6108*	0.1747
	Hemolysis vs. SMEs	0.0705	0.2312	0.7290*	0.2224
Senior Female (SF)	Hemolysis vs. MI	0.1712	0.2303	0.7032*	0.3898
	Hemolysis vs. SMEs	0.1797	0.3906	0.7346*	0.3311

**Table 1.** Correlations matrix (R squared values) between storage hemolysis and MIs, storage hemolysis and SMEs’ morphology subclass fractions. Strong correlations marked with “\*”.

females, the correlation remained low throughout the storage period, with the highest  $R^2$  value observed on Day 28 ( $R^2 = 0.1657$ ) (Fig. 2b). Teenage males exhibited a moderate correlation on Day 28 ( $R^2 = 0.4754$ ) and Day 42 ( $R^2 = 0.2748$ ) (Fig. 2a), suggesting a slight increase in the relationship between hemolysis and MIs over time.

The correlation between storage hemolysis and SMEs’ fraction followed a similar pattern across donor groups (Fig. 2e–h). For senior females, the correlation between hemolysis and SMEs’ fraction was strongest on Day 28 ( $R^2 = 0.7346$ ) (Fig. 2h) before decreasing slightly on Day 42 ( $R^2 = 0.3311$ ). Senior males also showed a strong positive correlation on Day 28 ( $R^2 = 0.7290$ ) (Fig. 2g), but this decreased by Day 42 ( $R^2 = 0.2224$ ). The teenage donor groups, however, exhibited less of a relationship between these two parameters. In teenage females, the relationship between hemolysis and SMEs’ fraction remained weak throughout the storage, with the highest  $R^2$  value seen on Day 42 ( $R^2 = 0.1446$ ) (Fig. 2f). Teenage males showed a moderate correlation on Day 28 ( $R^2 = 0.5261$ ) and Day 42 ( $R^2 = 0.4139$ ) (Fig. 2e), indicating a stronger relationship at later storage times.

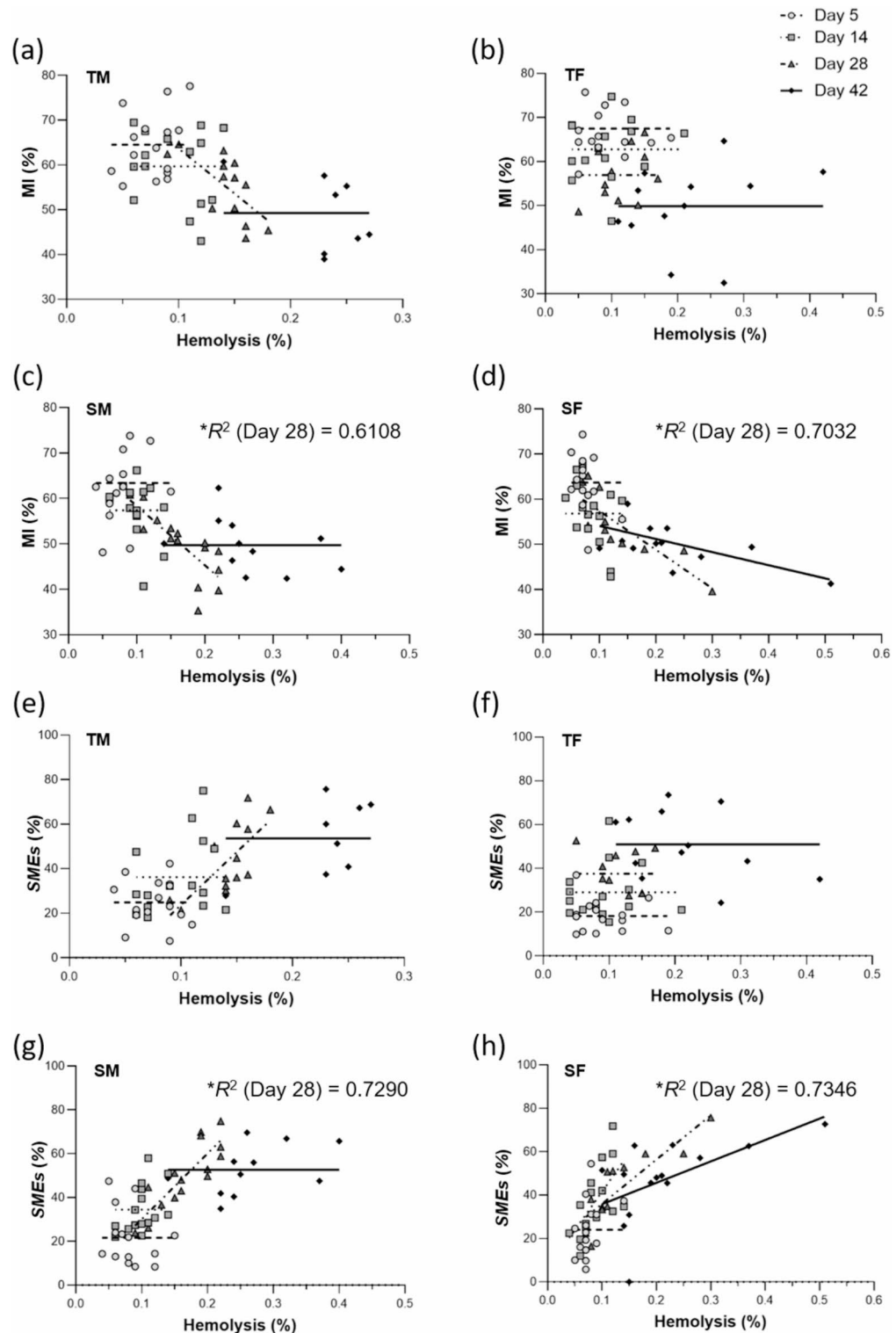


**Fig. 2.** The correlations between morphology and storage hemolysis. (a–d) The correlation between MIs and storage hemolysis determined for U-RBCs from: (a) teenage male (SM), (b) teenage female (TF), (c) senior male (SM), (d) senior female (SF) over hypothermic storage. (e–h) The correlation between SMEs' fraction and storage hemolysis determined for U-RBCs from: (e) TM, (f) TF, (g) SM, (h) SF. "MI" and "SMEs" indicate morphology index and storage-induced micro-erythrocytes, respectively. Strong correlations ( $R^2$  values > 0.5, day 28) is presented and marked with "x".



### The biological age of RBCs had a minimal impact on the distribution of RBC morphology subclasses

To study if biological age had any effect on the fractions of RBCs within each morphology subclass, images across the U-, Y- and O-RBCs subpopulations were compared. The differences in the subpopulations' RBC morphology subclass distributions were not significant across the entirety of hypothermic storage (Fig. 3). Y-RBCs exhibited a significantly higher fraction of crenated discoids than O- and/or U-RBCs during early storage ( $P < 0.05$ ) (Fig. 3a and b). However, this trend reversed after prolonged storage, with Y-RBCs possessing a lower fraction of crenated discoids by day 42 ( $P < 0.05$ ) (Fig. 3d). Conversely, O-RBCs displayed a higher fraction of crenated spheroids compared to Y- and U-RBCs on day 5 of storage ( $P < 0.05$ ) (Fig. 3a). After day 14 of cold storage though, O-RBCs were discovered to have a significantly lower fraction of crenated spheres than Y- and U-RBCs ( $P < 0.05$ ) (Fig. 3b and c, and d). Based on these findings, we examined more closely the three older subclasses (crenated spheroids, crenated spheres, and smooth spheres) or SMEs<sup>15</sup>. For RBCs from teenage males on day 5, SMEs' fraction in O-RBCs is higher than Y-RBCs ( $P < 0.01$ ) and U-RBCs ( $P < 0.05$ ). For RBCs from senior males and senior females on day 42, SMEs' fraction in O-RBCs is lower than Y-RBCs ( $P < 0.05$ ). At other time points during storage, the differences in the SMEs' fractions due to biological age were not statistically significant ( $P > 0.05$ ), even though the negative effects of storage lesions on morphology were still statistically discernible ( $P < 0.05$ ) (Fig. 4).

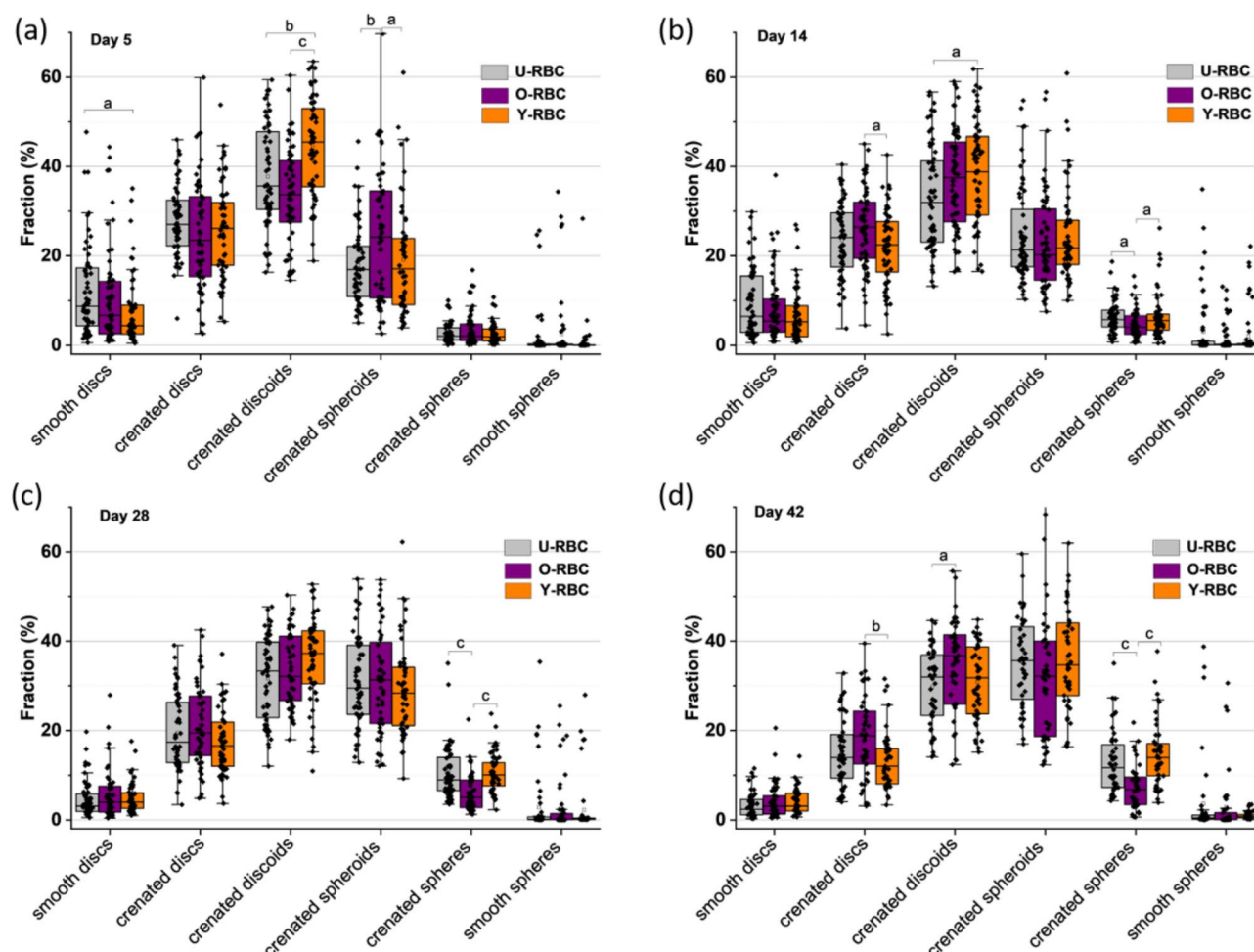


**Fig. 3.** Distribution of U-, O-, and Y-RBCs into morphology subclasses on (a) day 5, (b) day 14, (c) day 28, and (d) day 42 of storage. Medians are indicated as horizontal lines on the box and whisker plots. The box plot displays the average, median values, and the interquartile range (25 – 75%). The whiskers represent the range of extreme values, excluding outliers. (This applies to Figs. 4, 5, 6 and 7 as well). Lowercase letters from a to c on each solid line represent the significant difference between subpopulations of U-, O-, and Y-RBCs within each morphology subclass: a ( $P < 0.05$ ), b ( $P < 0.01$ ), c ( $P < 0.001$ ). Statistically significant difference levels between the three groups U-, O- and Y-RBCs (degree of freedom of 2) were calculated using the Tukey test and each group contains RBC images from all 60 donors.

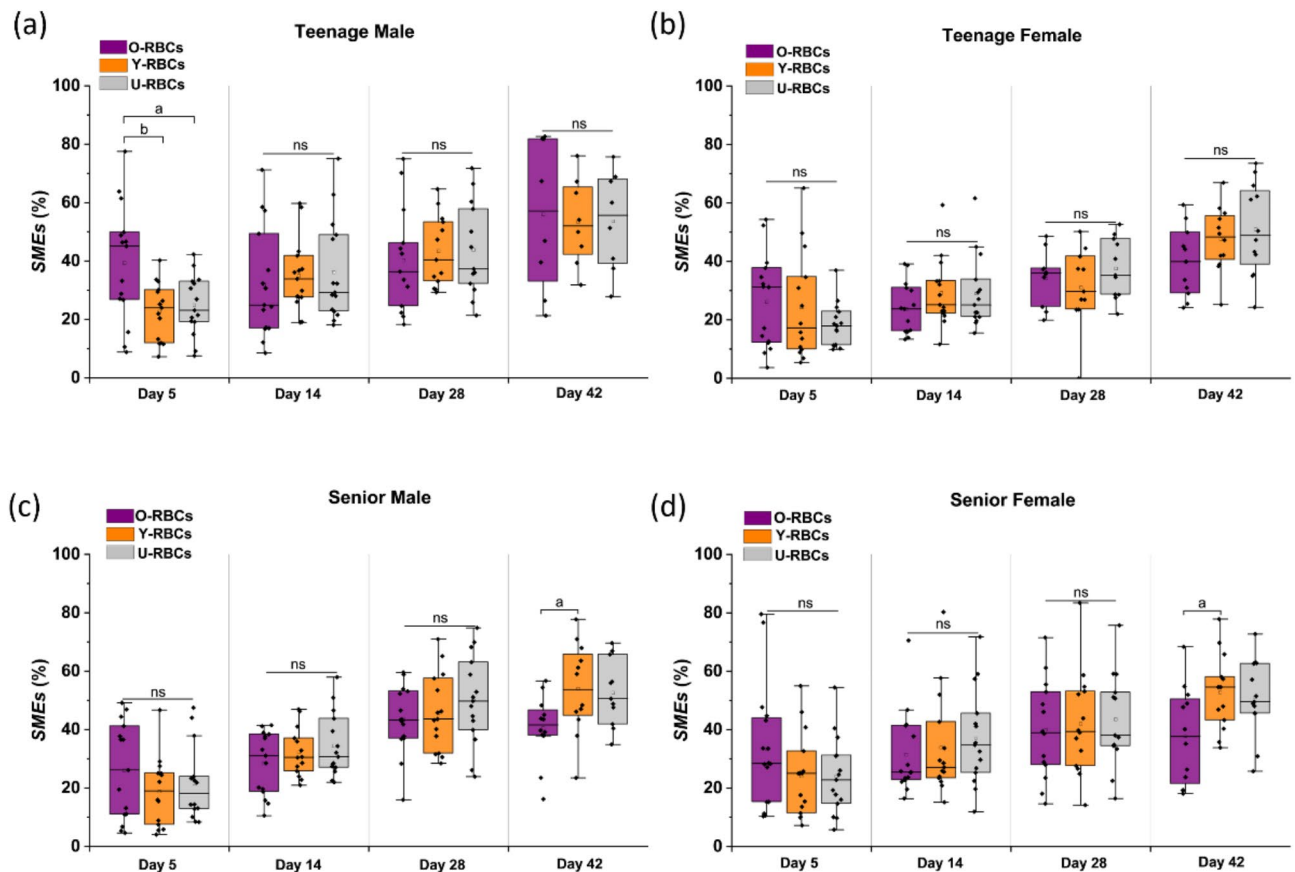


**Fig. 4.** SMEs' fractions (crenated spheroids, crenated spheres, and smooth spheres) across the biological age subpopulations for (a) teenage males, (b) teenage females, (c) senior males, and (d) senior females. Lowercase letters on each solid line represent the significant differences between subpopulations of U-, O-, and Y-RBCs at each time point of storage: ns (not significant  $P > 0.05$ ), a ( $P < 0.05$ ), b ( $P < 0.01$ ). Statistically significant difference levels between the three groups, U-, O- and Y-RBCs (degree of freedom of 2) were calculated using the Tukey test and each group contains RBC images from 15 donors.

### Hypothermic storage and donor age affect the distribution of RBC morphology subclasses significantly more than donor sex

RBCs were classified more into younger subclasses [e.g. smooth disc and crenated disc], on testing day 5 than at day 42, irrespective of the RBC subpopulation (Figs. 5 and S2). Unsurprisingly, SMEs' fractions also gradually increased over the course of storage from day 5 to day 42 ( $P < 0.05$ ) (Fig. 6). Interestingly, the increases in SMEs' fractions in senior female O-RBCs over hypothermic storage were not significant ( $P > 0.05$ ) (Fig. 6).

Notably, when morphology subclass fractions were stratified by donor characteristics, differences between teenage and senior donors were found to be significant (Fig. 5). On day 5, teenage male donors had a higher fraction of crenated spheres than teenage female donors within their U-RBCs, senior females within their O-RBCs, and both teenage females and senior males when only Y-RBCs were examined ( $P < 0.05$ ) (Fig. 5a and c, and Fig. 5e). Moreover, we found upon analyzing Y-RBCs, teenage and senior males had higher fractions of smooth spheres than teenage females ( $P < 0.05$ ) (Fig. 5). Also on day 42, O-RBCs from teenage male donors exhibited a significantly lower fraction of crenated discoids than all other donor groups ( $P < 0.05$ ) (Fig. 5d).

### MIIs were more significantly impacted by storage lesions than RBC biological age, donor sex or donor age

Determination of MIIs has provided a quantitative output to morphological assessments that is capable of capturing structural changes of RBCs that are associated with storage lesions or cellular senescence<sup>7,31</sup>. In alignment with the results found with the RBC morphology subclasses, RBC MIIs were more significantly affected by storage than donor factors (age and sex) regardless of their biological ages ( $P < 0.05$ ) (Fig. 7). The difference in calculated MIIs among U-, O-, and Y-RBCs was insignificant throughout most of storage, although the MIIs found for Y-RBCs were significantly higher than that of U- and O-RBCs on day 42 ( $P < 0.05$ ) (Fig. 7a). Notably the storage effects on MIIs, were most pronounced in U-RBCs and Y-RBCs, with no significant effects of storage discovered for teenage male and senior female O-RBCs ( $P < 0.05$ ) (Fig. 7b–d). The MIIs found for teen donors were significantly higher than senior donors on day 14 for U-RBCs and day 14 and day 28 for O-RBCs (Fig. S3).

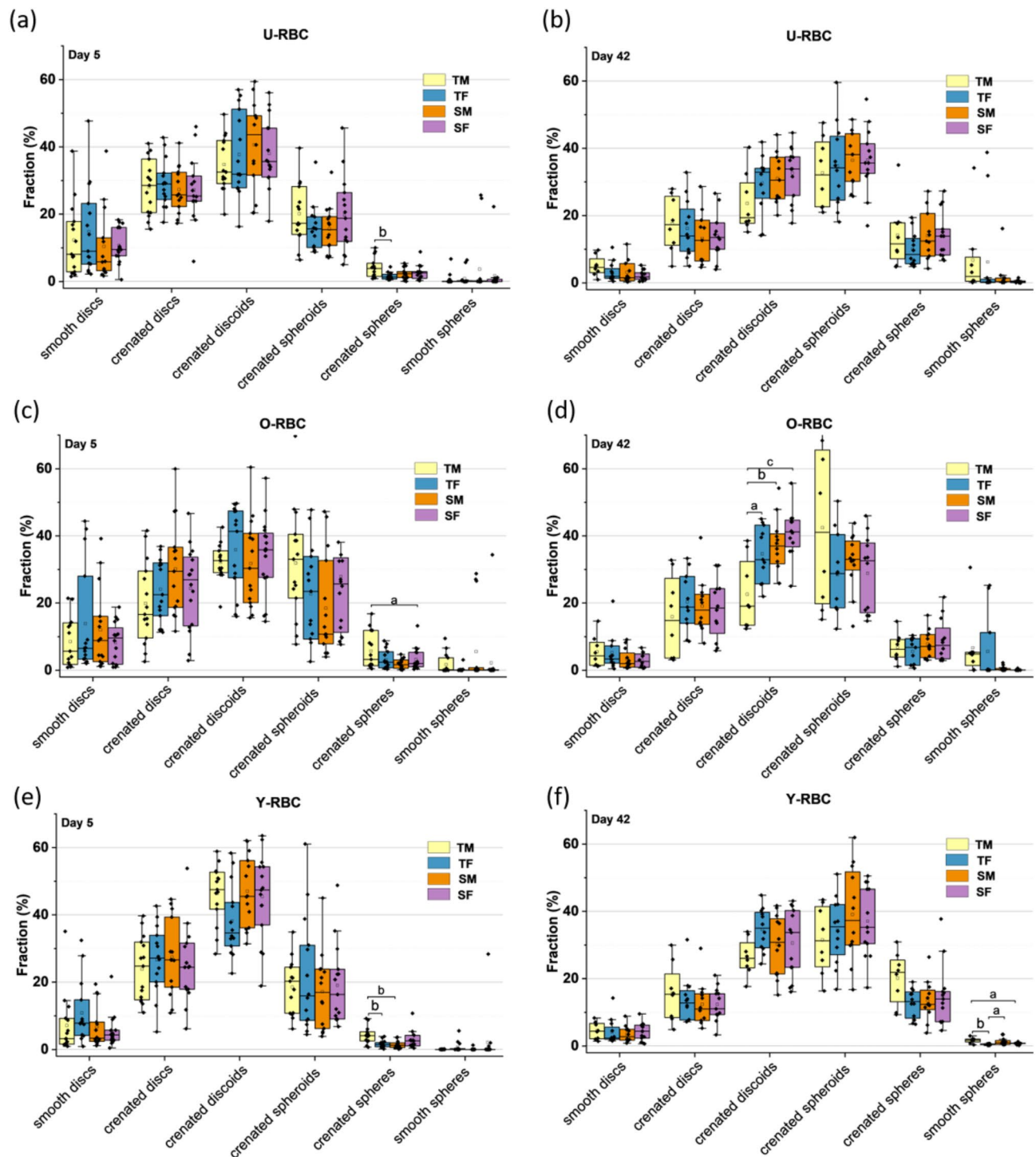


**Fig. 5.** Distribution of TM, TF, SM, and SF into morphology subclasses for (a) U-RBCs on day 5, (b) U-RBCs on day 42, (c) O-RBCs on day 5, (d) O-RBCs on day 42, (e) Y-RBCs on day 5, and (f) Y-RBCs on day 42 of storage. Lowercase letters from a to c on each solid line represent the significant differences between the donor characteristics of TM, TF, SM, and SF within each morphology subclass: a ( $P < 0.05$ ), b ( $P < 0.01$ ), c ( $P < 0.001$ ). Statistically significant difference levels between the four groups, TM, TF, SM, and SF (degree of freedom of 3) were calculated using the Tukey test and each group contains RBC images from 15 donors.

## Discussion

Morphology is a strong indicator of red cell function, closely linked to ion, energy, and redox homeostasis. Consequently, homeostatic derangement – through hypothermic storage or biological aging – is known to alter RBC morphology. Assessment of morphology can therefore be invaluable towards understanding the interplay between age-related changes in RBC function, tolerance to the stressors of hypothermic storage, and the donor-

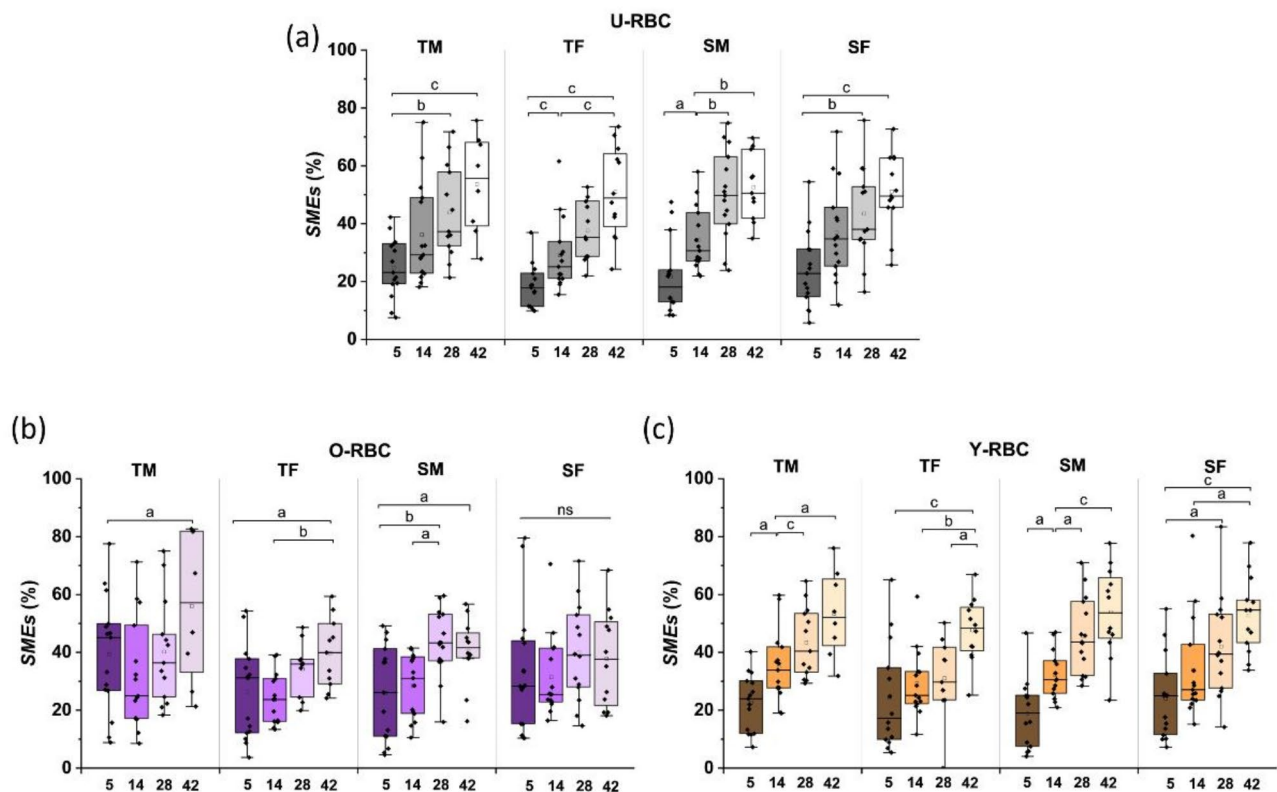


**Fig. 6.** SMEs' fractions stratified by donor characteristics (age and sex) for (a) U-RBCs, (b) O-RBCs, and (c) Y-RBCs. Statistically significant difference levels between the two groups were calculated using the Tukey test. Lowercase letters from a to c on each solid line represent the significant difference across storage within each donor characteristic: ns (not significant  $P > 0.05$ ), a ( $P < 0.05$ ), b ( $P < 0.01$ ), c ( $P < 0.001$ ). Statistically significant difference levels between the four timepoints of storage (degree of freedom of 3) were calculated using the Tukey test and each group contains RBC images from all 15 donors.

dependency of this relationship. Using a streamlined deep learning approach to classify RBCs into distinct morphology classes, we found that storage exerts the most significant impact on morphology, with donor characteristics, age and sex, and RBC biological age playing comparatively minor roles.

Degradation in the morphology of stored RBC is well-documented, and it is ultimately unsurprising within the design of our study that storage had the greatest impact<sup>32</sup>. While the totality of factors contributing to changes in RBC morphology remains incompletely understood, ATP is a key regulator, and its levels help explain why storage has a stronger impact than biological aging despite overlap in the metabolic sequelae of each parameter<sup>33</sup>. Elevated intracellular calcium levels, driven by ATP depletion, triggers chronic dehydration through activation of the KCa3.1 channel (i.e., the Gardos effect), promotes instability of critical cytoskeletal junctional complexes (e.g., spectrin-actin-tropomyosin, spectrin-actomyosin) through post-translational modifications on cytoskeletal adaptor proteins, and leads to activation of proteases (i.e. m-calpain or caspase) which degrade the cytoskeleton<sup>34</sup>. During storage, ATP levels drop by about 20% by day 28 and 40% by day 42, compared to a 10–20% decline as RBCs reach senescence over the course of ~120 days in vivo<sup>35,36</sup>. Moreover, beyond ATP depletion, the rise in intracellular calcium during storage is exacerbated by a ~60-fold reduction in the  $\text{Ca}^{2+}$  ATPase activity at hypothermic temperatures, leading to a 50–60% increase in calcium levels during storage, compared to a 10–30% rise during in vivo aging<sup>37–39</sup>. While metabolomics was not included initially in the design of this study, it would be worthwhile to investigate in the future, particularly to provide insight into the reduction in correlation between morphology and hemolysis evident in this study on day 42.

Although it is understandable that storage had a greater impact than biological aging, our results showed unexpectedly minor effects of biological age, with differences between subpopulations' morphology only emerging by day 42 (Fig. 7a). Our previous work revealed RCCs from teen male donors contained poor-quality biologically older cells<sup>40</sup>, and this work indicates that teenage male donors still demonstrated slightly more susceptibility to storage lesions. Our previous study also showed that rheological measurements are also not significantly influenced by biological age<sup>8,13,40</sup>. The metabolic superiority of young RBCs, including their ability to extrude calcium at nearly twice the rate of older cells, likely enhances their tolerance to the stressors of hypothermic storage, thereby reducing storage-induced morphological changes<sup>41</sup>. Additionally, younger RBCs are more resilient to late-stage disruptions in glutathione and methionine homeostasis occurring predominantly in the final two weeks of storage<sup>42</sup>. This improved ability to mitigate oxidative stress and repair isoparoyl protein



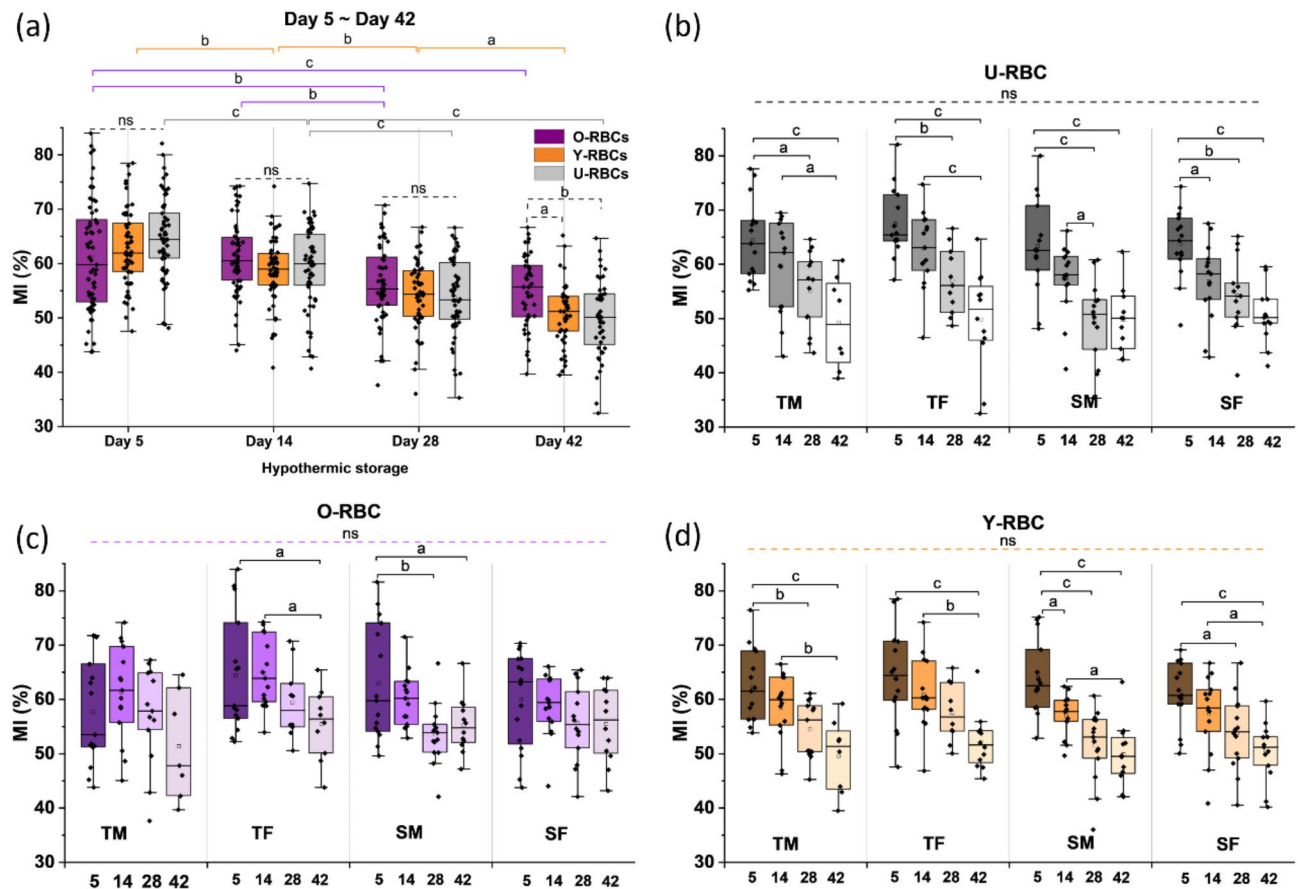


**Fig. 7.** MIs across the biological age subpopulations and donor characteristics (age and sex) throughout hypothermic storage from 5 to 42 days. (a) MIs across the biological age subpopulations from 5 to 42 days. MIs across donor characteristics (age and sex) for (b) U-RBCs, (c) O-RBCs, and (d) Y-RBCs. In (a), lowercase letters from a to c on each solid line represent the significant difference across storage within each subpopulation: a ( $P < 0.05$ ), b ( $P < 0.01$ ), c ( $P < 0.001$ ), where statistically significant difference levels (between four time points of storage with a degree of freedom of 3) were calculated using the Tukey test and each group contains RBC images from all 60 donors; lowercase letters from a to b on each dotted line represent the significant difference between subpopulations of U-, O-, and Y-RBCs at each time point of storage: ns (not significant  $P > 0.05$ ), a ( $P < 0.05$ ), b ( $P < 0.01$ ), where statistically significant difference levels (between three groups U-, O-, and Y-RBCs with a degree of freedom of 2) were calculated using the Tukey test and each group contains RBC images from all 60 donors. In (b–d), lowercase letters on each solid line represent the significant difference across storage within each donor characteristic: ns (not significant  $P > 0.05$ ), b ( $P < 0.01$ ), c ( $P < 0.001$ ), where statistically significant difference levels (between four time points of storage with a degree of freedom of 3) were calculated using the Tukey test and each group contains RBC images from 15 donors; lowercase letters on each dotted line represent the significant difference between TM, TF, SM, and SF at each time point of storage: ns (not significant  $P > 0.05$ ), b ( $P < 0.01$ ), c ( $P < 0.001$ ), where statistically significant difference levels (between four donor characteristics with a degree of freedom of 3) were calculated using the Tukey test and each group contains RBC images from 15 donors.

damage in response to oxidative stress may explain why morphological differences between the subpopulations would become more pronounced later in the storage period (Fig. 7a)<sup>43</sup>. However, the lack of morphological differences between subpopulations after isolation contrasts with previous studies using Percoll-separated RBCs<sup>44–46</sup>. We attribute this discrepancy to the size of the isolated subpopulations, particularly the young RBC group, which accounted for  $26.10 \pm 7.47\%$  of the total population. Recent research suggests RBCs begin transitioning to intermediate, reversible morphological stages within the first 2–3 weeks of their lifespan<sup>26,47</sup>. If we simply assume a 120-day lifespan and a linear relationship between density and RBC age, this suggests that the age of the RBCs in the young subpopulation isolated in this study ranged from 0 to 22 days at the lower estimate ( $26.10 \pm 7.47\%$ ) to 0–40 days at the upper estimate ( $26.10 \pm 7.47\%$ ). Thus, there is room to argue that these cells may have already undergone some degree of deleterious morphological changes, potentially obscuring detectable differences between subpopulations. This obfuscation could theoretically be exacerbated by the size of the old subpopulations ( $18.81 \pm 8.49\%$ ) given progression to SMEs morphologies (crenated spheroid, crenated sphere, and smooth sphere) is slow and generally occurs in the latter 2–3 weeks of the RBC lifespan<sup>47</sup>. Some limitations could also arise from the employment of IFC, which cannot capture the morphology of all cells

and consequently, the deep machine learning model classifies these cells as side view. A substantial portion of cells thereby are lost due to an inability of the deep machine learning model to recognize morphologies if the image inputs are not ideal. Regardless, given biological age had a minimal effect on morphology in this study, previously observed sex- and age-dependent differences in subpopulation proportions cannot fully explain the donor-dependent differences identified<sup>8</sup>.

Compared to storage conditions and biological aging, donor sex and age were expected to have the least impact on RBC morphology, as donor-to-donor differences may be influenced by multiple factors, including cytoskeletal elements, membrane proteins, enzyme polymorphisms, hemoglobin variants, RBC metabolism, redox status, as well as donor lifestyle and health status<sup>48,49</sup>. Donor age, previously was found to be a significant factor influencing the deformability of RBCs, regardless of biological age<sup>40</sup>. In this study, baseline measurements revealed no significant differences based on donor sex or age. However, by Day 14, MIs of teenage donors were significantly higher than that of seniors in unseparated RBC samples for both males and females, though this difference diminished at later time points. From a calcium homeostasis perspective, RBCs from seniors are known to have lower levels of calpastatin – the endogenous inhibitor of the calcium-activated m-calpain protease that promotes cytoskeletal degradation – possibly explaining this enhanced rate of early deterioration in morphology<sup>50,51</sup>. Another difference influenced by donor age is that the mean corpuscular volume in the male groups tended to increase with age<sup>13,52</sup>, which may impact the morphological evaluation undertaken in this study. Other anticipated donor-dependent differences in RBC quality, which could theoretically be aligned with morphology, were not reflected in our findings. For instance, despite evidence from our group and others that female RBCs generally store better than male RBCs, we found no significant sex-based differences, except for a slight, insignificant improvement in baseline (Day 5) MI in males<sup>53,54</sup>. Additionally, the protective effect of estrogen on RBCs of pre-menopausal females might suggest age-related MI differences between teenage pre-menopausal and senior post-menopausal females would be more pronounced than in males; however, this was not observed<sup>53</sup>.

While donor-dependent differences in morphology appeared minimal, it is essential to recognize the complexity of donor variability in RBCs, and the likelihood that classification solely by “sex” and “age” may be overly simplistic. This becomes evident when examining the wide range of morphology indices within each donor group, where the variability within groups likely negated the significance of many measures. Recent studies have emphasized the role of factors like ancestry, lifestyle, environmental exposures, and non-contraindicated pathologies in shaping donor-specific differences in RBC quality<sup>50,55,56</sup>. One key limitation of this study is the lack of detailed biochemical characterization of factors driving morphological changes, as well as the absence of secondary donor classification measures, which would provide a stronger framework for future research. Another limitation is that the Percoll density-based separation approach we employed involves washing in isotonic phosphate-buffered saline (PBS)<sup>8,13,28</sup>, leading to the shape of PBS-exposed RBCs resembling that of naturally occurring O-RBCs<sup>8,13,40,57</sup>. Also, PBS washing might result in stress-induced hemolysis<sup>8,13,40,57</sup>. Therefore, PBS exposure might introduce morphological alteration, affecting our interpretations.

The accuracy of our trained model was 84.17%, aligning with that reported in Doan et al. where the accuracy exceeded 70%<sup>23</sup>. The trained deep learning model achieved 84% agreement with experts, which means errors can still exist for the prediction results. Future work can be centered on further improving the deep learning framework of the neural network to obtain an even higher accuracy of the predicted results. The effects of donor characteristics and storage lesion on RBC quality can also be studied in more depth, focusing on with synergetic mechanisms with morphology and other quality factors, such as intracellular reactive oxygen<sup>7,8,28</sup>. Regarding the use of morphology as an indicator of RBC quality, correlations between previously obtained hemolysis metrics and MI values within donor subgroups were generally weak, except for the Day 28 results, which showed stronger correlations primarily among senior males and females (Fig. 2). Previously, mean corpuscular hemoglobin concentration and either estimated median densities or  $O_{Hyper}$  were also found to be strongly correlated in senior donors, hinting at the possibility of a quality parameter biomarker panel being developed for use in personalized transfusion medicine<sup>8,13</sup>. Our study demonstrates deep machine learning classification of RBC morphology could be another possible assay to aid in blood product decision making. By automating the classification of RBC shape, it could enhance both the efficiency and accuracy in predicting the deterioration of the RBCs due to morphological changes, potentially replacing traditional examination by microscopy. However, it is still potentially limited by upstream sample processing and acquisition.

In conclusion, a trained machine learning model was applied to predict the classification of unlabeled RBCs to investigate the morphology shapes of images of RBCs of 60 donors. Our data demonstrated storage has the most significant influence ( $P < 0.05$ ) on RBC morphology. Although RBC morphology differences across biological age were minimal until day 42, and teenage male donors still demonstrated slightly more susceptibility to storage lesions compared with senior males and females. This study underscores the significant impact of storage on morphology, highlighting storage as a key modifier of RBC quality and a likely mediator of adverse transfusion outcomes. The approach and outcome of this research has the potential to herald in a new era in RBC quality assessment.

## Methods

### Blood collection

CPD/SAGM units from 60 consenting donors were collected by the red cell filtration (RCF) method at Canadian Blood Services (Calgary, AB, Canada)<sup>8</sup>. RBCs originated from 15 teenage males (17–19 years old), 15 teenage females (17–19 years old), 15 senior males (75+ years old), and 15 senior females (75+ years old) (Fig. 1a). RBCs were obtained within 24 h of leuko-depletion (LD) and stored at 1–6 °C for 5, 14, 28, and 42 (+/- 3) days<sup>8</sup>.

### Storage hemolysis assay

The storage hemolysis of U-RBCs was measured over hypothermic storage (Day 5, 14, 28, and 42 ( $\pm 3$  days)) as described previously<sup>9</sup>. Briefly, hematocrit, total amount of sample hemoglobin before centrifugation, and levels of supernatant free hemoglobin obtained after centrifugation ( $\times 1500g$ , 10 min, 18 °C), were measured and used to calculate percent hemolysis<sup>7,9</sup>.

### Biological age profiling of RBCs by density gradient centrifugation

At four-time points (Day 5, 14, 28, and 42 ( $\pm 3$  days)) during hypothermic storage, Percoll (Percoll® GE Healthcare, Sigma-Aldrich, St. Louis, MO, US) density gradient centrifugations were performed to biologically age profile RBCs into more dense and less dense subpopulations<sup>8,13</sup>. After centrifugation, RBCs were separated into two subpopulations: the bottom layer ( $18.81 \pm 8.49\%$ ) consisting of dense, more senescent, older RBCs (“old”, O-RBCs), and the top layer ( $26.10 \pm 7.47\%$ ) containing the less dense, younger RBCs (“young”, Y-RBCs). These subpopulations consisting purely of cells at the extreme ends of biological aging served as the samples run on the imaging flow cytometer. A portion of unseparated RBCs (U-RBCs) was also retained for evaluation as a control alongside the young and old subpopulations (Fig. 1a).

### Imaging flow cytometry (IFC)

To obtain images of the U-, O- and Y-RBCs from 60 donors, an imaging flow cytometer (Amnis ImageStreamX Mark II, EMD Millipore, Seattle, WA) (Fig. 1a), with a four-laser two-camera system (ASSIST calibrated), was employed<sup>7</sup>. Approximately 10, 000–30, 000 RBC images per sample were captured across three channels (Channels 1, 9 (bright field), and 12 (dark field)) using the low-speed/high-sensitivity settings at 60 $\times$  image magnification. The acquired raw images for each sample were preliminarily processed using the IDEAS software platform (Version 6.2, EMD Millipore) to remove out-of-focus cells, artifacts, debris, and clumped objects, and finally saved in “.tif” format for downstream deep-learning analysis<sup>11,23,58</sup>.

### Training of the machine learning model

The Deepometry program was run on the Google Cloud Platform to train a deep machine learning model following a previously developed machine learning framework by Doan et al.<sup>23</sup> First, the raw manually labeled dataset of images published in<sup>23</sup> was used for supervised training. Briefly, RBCs obtained from day 2 to day 42 of storage were manually annotated by assigned human annotators, in consultation with a morphology expert into each subclass of RBC morphology: smooth disc, crenated disc, crenated discoid, crenated spheroid, crenated sphere, smooth sphere, and side view<sup>23</sup>. Raw images were transferred from “.tif” into “.mat” format for the preprocessing of images, similar to the previously established label-free imaging flow cytometry machine vision framework<sup>11,23,58</sup>. Then, the model was supervised deep trained for a maximum of 512 epochs. The machine learning training process is outlined in Fig. S1. During the supervised training process, accuracy was monitored in real-time. The trained model is capable of classifying RBC images into the six different morphology subclasses (smooth disc, crenated disc, crenated discoid, crenated spheroid, crenated sphere, smooth sphere), plus an additional subclass labeled as side-view where the true class is indiscernible due to the limitations of IFC (Fig. 1b). After the classifier model had been trained, the accuracy of the trained model is evaluated using the trained database manually labeled and 20% of images split from the database. Additionally, another three different groups of labeled datasets were used for the evaluation of the accuracy of the trained model to control for overfitting (see Data Availability).

### Machine learning model prediction

The trained model was applied to predict the morphology of images of RBCs obtained from 60 donors (15 teenage males, 15 teenage females, 15 senior males, 15 senior females) and separated based on their biological age (U-, O-, and Y-RBCs) at 4 different storage time points (Day 5, 14, 28 and 42 ( $\pm 3$  days)). The percentage of each subclass of morphology (fraction) was calculated using the equation below

$$P (\%) = \frac{N (\text{subclass})}{N (\text{total}) - N (\text{sideview})} \times 100\% \quad (1)$$

where  $P (\%)$  is the portion percentage of each subclass morphology (smooth disc, crenated disc, crenated discoid, crenated spheroid, crenated sphere, and smooth sphere).  $N (\text{subclass})$  represents the number of each subclass morphology.  $N (\text{total})$  is the total number of RBCs for each group. And  $N (\text{sideview})$  refers to the number of cells whose true class was indiscernible and annotated as side view, which is removed from the total number of cells. The proportion of subclass classified as side view in each sample was approximately  $18.98\% \pm 7.43\%$  (mean  $\pm$  standard deviation, see Fig. S4), and these were excluded from each sample.

Morphology indices (MIs) were calculated by multiplying the fraction of different morphology subclasses (obtained by Eq. 1) by their corresponding shape factors (1.0, 0.8, 0.6, 0.4, 0.2, and 0.0, respectively): smooth discs (SDC), crenated discs (CDC), crenated discoids (CDD), crenated spheroids (CSD), crenated spheres (CSE), smooth spheres (SSE). Previously developed, the detailed estimation equation is as follows<sup>7</sup>

$$MI = \frac{SDC \times 1.0 + CDC \times 0.8 + CDD \times 0.6 + CSD \times 0.4 + CSE \times 0.2 + SSE \times 0.0}{SDC + CDC + CDD + CSD + CSE + SSE} \times 100\% \quad (2)$$

### Data analysis

The mean value and the corresponding standard deviation of each condition were calculated with the software: OriginLab 2024 (OriginLab Corporation). One-way ANOVA analysis was performed to test significant

differences between experimental groups using the Tukey test. Three significant difference levels ( $P < 0.05$ ,  $P < 0.01$ ,  $P < 0.001$ ) were evaluated. This type of statistical testing was performed to ascertain the value of model accuracy, the portion percentage of each subclass morphology  $P$  (%), and morphology index MI (%). The overall ANOVA  $F$  value and  $P$  values in each figure are listed in the Supplementary Information. Correlations between storage hemolysis and MI or SMEs' fraction were assessed using a linear regression model and measured by the coefficient of determination ( $R^2$ ).  $R^2$  values less than 0.3 indicated a weak relationship, values between 0.3 and 0.7 indicated a moderate correlation, and values exceeding 0.7 indicated a very strong relationship.

## Data availability

Annotated data of RBC cells for supervised learning can be found in Figshare ([https://figshare.com/articles/software/Expert\\_Annotated\\_RBC/13053968](https://figshare.com/articles/software/Expert_Annotated_RBC/13053968)). Annotated data of RBC cells for evaluation of the trained model can be found in Figshare ([https://figshare.com/articles/figure/URL7\\_Annotated\\_Data/12432506](https://figshare.com/articles/figure/URL7_Annotated_Data/12432506)). The images from 60 donors during hypothermic storage used for prediction can be found at [https://drive.google.com/drive/folders/1NxV2W-aUcoB0W\\_DQKJWayDTN3rY67XFB](https://drive.google.com/drive/folders/1NxV2W-aUcoB0W_DQKJWayDTN3rY67XFB).

Received: 28 October 2024; Accepted: 17 February 2025

Published online: 05 March 2025

## References

- Pandey, S. et al. Intermittent scavenging of storage lesion from stored red blood cells by electrospun nanofibrous sheets enhances their quality and shelf-life. *Nat. Commun.* **13**, 7394. <https://doi.org/10.1038/s41467-022-35269-3> (2022).
- Sparrow, R. L. Red blood cell storage and transfusion-related immunomodulation. *Blood Transfus.* **8**, 26–30. <https://doi.org/10.2450/2010.005S> (2010).
- Dybas, J. et al. Label-free testing strategy to evaluate packed red blood cell quality before transfusion to leukemia patients. *Sci. Rep.* **12**, 21849 (2022).
- World Health Organization. Blood safety and availability. (2023). Available from <https://www.who.int/news-room/fact-sheets/detail/blood-safety-and-availability>
- World Health Organization. Global status report on blood safety and availability. (2016). Available from: <https://www.who.int/publications/book-orders>
- Yoshida, T. et al. Enhancing uniformity and overall quality of red cell concentrate with anaerobic storage. *Blood Transfus.* **15**, 172–181 (2017).
- Mykhailova, O., Olafson, C., Turner, T. R., D' Alessandro, A. & Acker, J. P. Donor-dependent aging of young and old red blood cell subpopulations: Metabolic and functional heterogeneity. *Transfusion* **60**, 2633–2646 (2020).
- Mykhailova, O. et al. Estimated median density identifies donor age and sex differences in red blood cell biological age. *Transfusion* **64**, 705–715 (2024).
- Cloutier, M. et al. Quality assessment of red blood cell concentrates from blood donors at the extremes of the age spectrum: The BEST collaborative study. *Transfusion* **63**, 1506–1518 (2023).
- Roussel, C. et al. Spherocytic shift of red blood cells during storage provides a quantitative whole cell-based marker of the storage lesion. *Transfusion* **57**, 1007–1018 (2017).
- Doan, M. et al. Objective assessment of stored blood quality by deep learning. *Proc. Natl. Acad. Sci. U S A.* **117**, 21381–21390 (2020).
- Longster, G. H., Buckley, T., Sikorski, J. & Tovey, L. A. D. scanning electron microscope studies of red cell morphology: changes occurring in red cell shape during storage and post transfusion. *Vox Sang.* **22**, 161–170 (1972).
- Mykhailova, O. et al. Red cell concentrates from teen male donors contain poor-quality biologically older cells. *Vox Sang.* **119**, 417–427 (2024).
- Zhong, R. et al. An evaluation of morphological changes and deformability of suspended red blood cells prepared using whole blood with different hemoglobin levels of tibetans. *Transfus. Med. Hemotherapy.* **48**, 210–219 (2021).
- Roussel, C. et al. Rapid clearance of storage-induced microerythrocytes alters transfusion recovery. *Blood* **137**, 2285–2298 (2021).
- D'Alessandro, A. & Liunbruno, G. M. Red blood cell storage and clinical outcomes: New insights. *Blood Transfusion* **15**, 101–103 (2017). <https://doi.org/10.2450/2017.0018-17>
- D'Alessandro, A. et al. An update on red blood cell storage lesions, as gleaned through biochemistry and omics technologies. *Transfusion* **55**, 205–219. <https://doi.org/10.1111/trf.12804> (2015).
- Harmon, S. A., Tuncer, S., Sanford, T., Choyke, P. L. & Türkbe, B. Artificial intelligence at the intersection of pathology and radiology in prostate cancer. *Diagn. Interv. Radiol.* **25**, 183–188 (2019).
- Gorman, C. et al. Interoperable slide microscopy viewer and annotation tool for imaging data science and computational pathology. *Nat. Commun.* **14**, 1572 (2023).
- Busnatu, Ş. et al. Clinical applications of Artificial Intelligence—An updated overview. *J. Clin. Med.* **11**, 2265. <https://doi.org/10.3390/jcm11082265> (2022).
- Gedefaw, L. et al. Artificial Intelligence-assisted diagnostic cytology and genomic testing for hematologic disorders. *Cells* **12**, 1755. <https://doi.org/10.3390/cells12131755> (2023).
- Wong, A. N. N. et al. Current developments of Artificial Intelligence in digital pathology and its future clinical applications in gastrointestinal cancers. *Cancers* **14**, 3780. <https://doi.org/10.3390/cancers14153780> (2022).
- Doan, M. et al. Deepometry, a framework for applying supervised and weakly supervised deep learning to imaging cytometry. *Nat. Protoc.* **16**, 3572–3595 (2021).
- Pinto, R. N. et al. Label-free analysis of red blood cell storage lesions using imaging flow cytometry. *Cytom Part. A.* **95**, 976–984 (2019).
- Routt, A. H., Yang, N., Piety, N. Z., Lu, M. & Shevkopyas, S. S. Deep ensemble learning enables highly accurate classification of stored red blood cell morphology. *Sci. Rep.* **13**, 1–15 (2023).
- Huang, Y. X. et al. Human red blood cell aging: Correlative changes in surface charge and cell properties. *J. Cell. Mol. Med.* **15**, 2634–2642 (2011).
- Hogman, C. F. & Meryman, H. T. Storage parameters affecting red blood cell survival and function after transfusion. *Transfus. Med. Rev.* **13**, 275–296 (1999).
- Zimrin, A. B. & Hess, J. R. Current issues relating to the transfusion of stored red blood cells. *Vox Sang.* **96**, 93–103. <https://doi.org/10.1111/j.1423-0410.2008.01117.x> (2009).
- Buczak, A. L. & Guven, E. A survey of data mining and machine learning methods for cyber security intrusion detection. *IEEE Commun. Surv. Tutorials.* **18**, 1153–1176 (2016).
- Goodfellow, I., Bengio, Y. & Courville, A. *Deep Learning* (The MIT Press, 2016). [www.deeplearningbook.org](http://www.deeplearningbook.org)



31. Tchir, J. D. R., Acker, J. P. & Holovati, J. L. Rejuvenation of ATP during storage does not reverse effects of the hypothermic storage lesion. *Transfusion* **53**, 3184–3191 (2013).
32. Blasi, B., D'Alessandro, A., Ramundo, N. & Zolla, L. Red blood cell storage and cell morphology. *Transfus. Med.* **22**, 90–96 (2012).
33. Bull, B. S. & Brailsford D. Red blood cell shape, Red Blood Cell Membranes. (CRC Press. Taylor Fr. Boca Rat. FL, 2020). <https://doi.org/10.1201/9781003066118>
34. Bogdanova, A., Makhro, A., Wang, J., Lipp, P. & Kaestner, L. Calcium in red blood cells—a perilous balance. *Int. J. Mol. Sci.* **14**, 9848–9872. <https://doi.org/10.3390/ijms14059848> (2013).
35. Lagerberg, J. W., Korsten, H., Van Der Meer, P. F. & De Korte, D. Prevention of red cell storage lesion: A comparison of five different additive solutions. *Blood Transfus.* **15**, 456–462 (2017).
36. Magnani, M. et al. The age-dependent metabolic decline of the red blood cell. *Mech. Ageing Dev.* **22**, 295–308 (1983).
37. Sarkadi, B., Szász, I., Gerlóczy, A. & Gárdos, G. Transport parameters and stoichiometry of active calcium ion extrusion in intact human red cells. *BBA - Biomembr.* **464**, 93–107 (1977).
38. Gevi, F., D'Alessandro, A., Rinalducci, S. & Zolla, L. Alterations of red blood cell metabolome during cold liquid storage of erythrocyte concentrates in CPD-SAGM. *J. Proteom.* **76**, 168–180 (2012).
39. Samaja, M., Rubinacci, A., Motterlini, R., De Ponti, A. & Portinaro, N. Red cell aging and active calcium transport. *Exp. Gerontol.* **25**, 279–286 (1990).
40. Olga Mykhailova, M. et al. J. P. A. Donor age more than donor sex and red blood cell biological age contributes to the rheological properties of stored red cell concentrates. *Blood Adv.* In submission, (2024).
41. Romero, P. J. & Romero, E. A. Differences in  $\text{Ca}^{2+}$  pumping activity between sub-populations of human red cells. *Cell. Calcium.* **21**, 353–358 (1997).
42. Bordbar, A. et al. Identified metabolic signature for assessing red blood cell unit quality is associated with endothelial damage markers and clinical outcomes. *Transfusion* **56**, 852–862 (2016).
43. Levine, R. L., Berlett, B. S., Moskovitz, J., Mosoni, L. & Stadtman, E. R. Methionine residues may protect proteins from critical oxidative damage. *Mech. Ageing Dev.* **107**, 323–332 (1999).
44. Gifford, S. C., Derganc, J., Shevkopyas, S. S., Yoshida, T. & Bitensky, M. W. A detailed study of time-dependent changes in human red blood cells: From reticulocyte maturation to erythrocyte senescence. *Br. J. Haematol.* **135**, 395–404 (2006).
45. Waugh, R. E. et al. Rheologic properties of senescent erythrocytes: Loss of surface area and volume with red blood cell age. *Blood* **79**, 1351–1358 (1992).
46. Baryn, M. et al. Red blood cells ageing markers: A multi-parametric analysis. *Blood Transfus.* **15**, 239–248 (2017).
47. Minetti, G., Achilli, C., Perotti, C. & Ciana, A. Continuous change in membrane and membrane-skeleton organization during development from proerythroblast to senescent red blood cell. *Front. Physiol.* **9**, 286. <https://doi.org/10.3389/fphys.2018> (2018).
48. Hadjesfandiari, N., Khorshidfar, M. & Devine, D. V. Current understanding of the relationship between blood donor variability and blood component quality. *Int. J. Mol. Sci.* **22**, 3943 (2021).
49. D'Alessandro, A. et al. Donor sex, age and ethnicity impact stored red blood cell antioxidant metabolism through mechanisms in part explained by glucose 6-phosphate dehydrogenase levels and activity. *Haematologica* **106**, 1290–1302 (2021).
50. Yadav, S., Maurya, P. K. & Deepika, A. A systematic review of red blood cells biomarkers in human aging. *Journals Gerontol. - Ser. Biol. Sci. Med. Sci.* **79**, glae004 (2024).
51. Schwarz-Benmeir, N., Glaser, T., Barnoy, S. & Kosower, N. S. Calpastatin in erythrocytes of young and old individuals. *Biochem. J.* **304**, 365–370 (1994).
52. Pluncevic Gligoroska, J. et al. Red blood cell variables in children and adolescents regarding the age and sex. *Iran. J. Public. Health.* **48**, 704–712 (2019).
53. Tzounakas, V. L. et al. Sex-related aspects of the red blood cell storage lesion. *Blood Transfus.* **19**, 224–236 (2021).
54. Daly, A., Raval, J. S., Waters, J. H., Yazer, M. H. & Kameneva, M. V. Effect of blood bank storage on the rheological properties of male and female donor red blood cells. *Clin. Hemorheol Microcirc.* **56**, 337–345 (2014).
55. Kanas, T. et al. Ethnicity, sex, and age are determinants of red blood cell storage and stress hemolysis: Results of the REDS-III RBC-Omics study. *Blood Adv.* **1**, 1132–1141 (2017).
56. Sparrow, R. L., Payne, K. A. & Adams, G. G. Higher donor body mass index is associated with increased hemolysis of red blood cells at 42-days of storage: A retrospective analysis of routine quality control data. *Transfusion* **61**, 449–463 (2021).
57. Son, M. et al. Effects of osmolality and solutes on the morphology of red blood cells according to three-dimensional refractive index tomography. *PLoS One.* **16**, e0262106 (2021).
58. Doan, M. et al. Label-free leukemia monitoring by computer vision. *Cytom Part. A.* **97**, 407–414 (2020).

## Acknowledgements

We are grateful to Canadian Blood Services' blood donors who made this research possible. Yuanheng Zhao and Olga Mykhailova were supported by a Post-Doctoral Fellowships from Canadian Blood Services. We would like to acknowledge Celina Phan, April Xu, and Carly Olafson with their work on hemolysis testing and Percoll separations. We thank the flow cytometry facility in the Faculty of Medicine & Dentistry at the University of Alberta who assisted with the IFC data acquisition. Special thanks to Dr Minh Doan from the Broad Institute of Harvard and MIT and Dr Claire Barnes from Swansea University who assisted with the set-up of the deep machine learning framework.

## Author contributions

YHZ performed deep machine learning data analysis, data interpretation, and was integral to manuscript writing. OM was responsible for study design, data collection, data interpretation, in addition to drafting and reviewing the manuscript. MBC was involved with data analysis and data interpretation in addition to manuscript writing and reviewing. MY was involved in part of data analysis, data interpretation and the manuscript writing process. NW assisted with data collection, data interpretation, and the manuscript writing process. RO assisted with data collection, and the manuscript writing process. TK and JA were integral in study design, data interpretation, and manuscript reviewing.

## Declarations

## Competing interests

The authors declare no competing interests.

### Additional information

**Supplementary Information** The online version contains supplementary material available at <https://doi.org/10.1038/s41598-025-90760-3>.

**Correspondence** and requests for materials should be addressed to J.P.A.

**Reprints and permissions information** is available at [www.nature.com/reprints](http://www.nature.com/reprints).

**Publisher's note** Springer Nature remains neutral with regard to jurisdictional claims in published maps and institutional affiliations.

**Open Access** This article is licensed under a Creative Commons Attribution-NonCommercial-NoDerivatives 4.0 International License, which permits any non-commercial use, sharing, distribution and reproduction in any medium or format, as long as you give appropriate credit to the original author(s) and the source, provide a link to the Creative Commons licence, and indicate if you modified the licensed material. You do not have permission under this licence to share adapted material derived from this article or parts of it. The images or other third party material in this article are included in the article's Creative Commons licence, unless indicated otherwise in a credit line to the material. If material is not included in the article's Creative Commons licence and your intended use is not permitted by statutory regulation or exceeds the permitted use, you will need to obtain permission directly from the copyright holder. To view a copy of this licence, visit <http://creativecommons.org/licenses/by-nc-nd/4.0/>.

© The Author(s) 2025